Plasmonic Ruler at the Liquid–Liquid Interface

Vladimir A. Turek, Michael P. Cecchini, Jack Paget, Anthony R. Kucernak, Alexei A. Kornyshev,* and Joshua B. Edel*

Department of Chemistry, Chemical Physics Section, Imperial College London, Exhibition Road, South Kensington, London, SW7 2AZ, United Kingdom

ABSTRACT We report on a simple, fast, and inexpensive method to study adsorption and desorption of metallic nanoparticles at a liquid/liquid interface. These interfaces provide an ideal platform for the formation of two-dimensional monolayers of nanoparticles, as they form spontaneously and are defect-correcting, acting as 2D "nanoparticle traps". Such two-dimensional, self-assembled nanoparticle arrays have a vast range of potential applications in displays, catalysis, plasmonic rulers, optoelectronics, sensors, and detectors. Here, we show that 16 nm diameter gold nanoparticles can be controllably adsorbed to a water/1,2-dichloroethane interface, and that we can control the average interparticle spacing at the interface over the range 6–35 nm. The particle density and average interparticle spacing are experimentally assessed by measuring the optical plasmonic response of the nanoparticles in the bulk and at the interface and by comparing the experimental data with existing theoretical results.

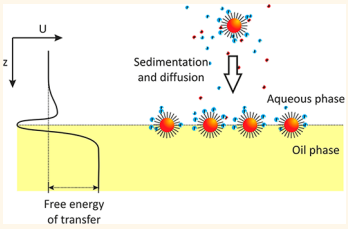

KEYWORDS: liquid–liquid interface · plasmonic ruler · nanoparticles · self assembly · centrifugation

Nanoparticle (NP) adsorption at liquid–liquid interfaces (LLIs) is a well-established phenomenon that was first reported independently more than a century ago by Ramsden and Pickering.[1,2] More recently, plasmonic NPs at LLIs have been reported to possess novel "metal liquid like" properties[3] that have sparked a renewed interest. Driven by the growing need for cheap, fast and reproducible bottom-up assembly for nanotechnological applications, the unique optical,[4] magnetic,[5] electrical,[6] and chemical[7] properties of such films has attracted intensive research in a rapidly growing field.

NP assemblies at the LLI hold great promise in diverse fields ranging from electrovariable optics[8] to templates for hierarchical self-assembly,[9] and plasmonic rulers.[10] One of the main benefits of localizing NPs at a LLI for these applications is the aforementioned self-assembly.[11] Currently, most technological applications of nanoassemblies are based around solid-state fabrication. Although the control that the solid interface offers is unparalleled, it does have several drawbacks when compared to a LLI. One such drawback is topological defects which can emerge either during or post-manufacturing and are extremely difficult to correct. In fact, it is often easier to fabricate a new device rather than attempting to repair defects. Inversely, a LLI system has the ability to self-correct without any external manipulation.[12]

An additional drawback of a solid state system becomes clear when introducing the exciting concept of a plasmonic ruler.[13–15] Precise NP spatial information can be extracted through localized plasmon coupling. This concept has been demonstrated for 2D arrays,[10] particle dimers[14] at solid interfaces and tethered NPs in bulk solution.[16] The plasmonic ruler has even recently been demonstrated to provide 3-dimensional structural information.[17] The use of plasmonic particles at the LLI should therefore provide information on the structural characteristics of these assemblies. The large body of work on plasmonic NPs at LLIs has typically focused on close packed arrays and is broadly divided into spectroscopic studies for sensing[18,19] (e.g., SERS and SPR) or use of the LLI as a template for 2D self-assembly.[20]

Despite our growing theoretical understanding of these assemblies,[21] there are numerous questions that remain unanswered. It has become evident through theory,[22,23] simulation,[24,25] and key experiments[26–28] that the simple electrostatic and van der Waals forces that DLVO (Derjaguin–Landau–Verwey–Overbeek) theory considers for NPs in bulk solution is not sufficient to explain the stability of NPs at the LLI. NP interactions at the LLI are governed by interfacial tension stabilization,[8] long-range dipole–dipole interactions resulting from an asymmetric counterion cloud,[29] hydration forces for the NP immersed in the two fluids,[30] capillary forces

* Address correspondence to a.kornyshev@imperial.ac.uk, joshua.edel@imperial.ac.uk.

Received for review April 22, 2012 and accepted August 19, 2012.

Published online August 19, 2012
10.1021/nn302941k

resulting from deformations of the interface,[31] van der Waals forces that differ to those in the bulk,[32] as well as thermal fluctuations.[33] It is beyond the scope of this work to give a detailed account of these forces, especially when comprehensive review articles have been published on these interactions.[11,34,35] However, for clarity the balance of forces and a pictorial representation of NP adsorption to the LLI are shown in Figure 1.

From an experimental perspective, characterizing these interfaces can be a challenging task. For example, invaluable insight has come from experiments utilizing grazing-incidence small-angle X-ray scattering to study the assembly of small CdSe nanocrystals at a toluene–water interface[36] in which it was determined that the particles form a close packed, but disordered liquid-like structure. Furthermore, fluorescence loss induced by photobleaching and fluorescence recovery after photobleaching on the same system revealed that the lateral diffusion of these assemblies is four orders of magnitude slower than its bulk counterpart.[36] Second harmonic generation,[37] surface plasmon resonance,[38] and ellipsometry[39] have also been shown as characterization methods for NPs at the LLI. More recently, freeze-fracture shadow-casting cryo SEM has been performed with single-particle resolution.[40] However, most of these techniques are time-consuming and require specialized equipment. Therefore a need exists for a fast, *in situ* technique that would extract, with nanometer resolution, the structural characteristics of these films.

In this paper we develop techniques for characterizing and controlling the spacing of NPs at a LLI. To use the plasmon ruler at these interfaces, one needs to first control the adsorption of NPs to the LLI and prevent aggregation-induced close packing. Diffusion-driven, electrochemical,[41] and ethanol-induced[42] adsorption to the liquid interface are among the most widely used strategies. Out of these techniques, spontaneous self-assembly is the most convenient for the plasmon ruler; however, the assembly time is generally limited by diffusion. We build on this by using centrifugation as a means to adsorb a 2D array of 16 nm Au NPs to a water/1,2-dichloroethane (DCE) LLI. Spectroscopic techniques are used to characterize the plasmonic properties of the NPs by controlling the centrifugal force, centrifugation time, salt concentration, interfacial area, and pH. The methods utilized are simple, fast, and inexpensive and can be used to characterize and control the properties of NPs at the LLI.

RESULTS AND DISCUSSION

Centrifugation as a Means of Kinetic Control of NP Assembly at the LLI. The simplicity and flexibility of centrifugation makes it an ideal technique to control particle adsorption to the LLI. We will forego a comprehensive study on the effects of centrifugation of the NPs, focusing instead on the experimental observation arising from NP assembly, disassembly, and controlled spacing at the LLI. The reader is referred to the Supporting Information for a detailed discussion on the physical background behind centrifugation speed and time dependence on NP adsorption.

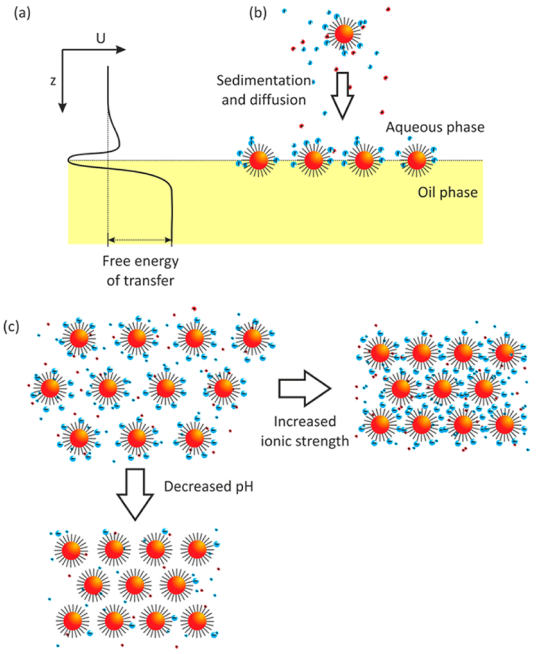

Figure 1. The main factors that influence localization of NPs functionalized by charged ligands at the LLI. (a) The free energy profile, *U*(*z*), for a single NP at the LLI is dominated by an interfacial stabilization well caused by the reduction of the system free energy when the NP blocks some parts of the energetically unfavorable interface between the aqueous and organic phases. For highly charged NPs, the combination of interfacial stabilization and Born resolvation may give rise to a barrier on the aqueous side separating the well. The ratio of the height of the barrier to the depth of the well should grow with the size of the NP, as long as the amount of charge on an NP scales as its surface area. (b) The particles reside on the interface driven by the interfacial stabilization, but they feel this force at the distances of the order of their size. (c) NPs at the water/oil interface with a viewpoint normal to it. The interparticle separation is controlled by the ionic strength of the solution and also the charge on the particles, which is controlled by the pH of the solution, and ligand functionality.

Unless otherwise stated, the procedure for NP assembly describing all the steps is shown in Tables 1 and 2. A general experimental schematic of the protocol for assembly and the detection of the NPs at the LLI are shown in Figure 2. After centrifugation, all but 100 μL of the aqueous solution was removed. This resulted in the 100 μL solution forming a droplet with the assembled NPs at the DCE/aqueous boundary. Notably, a distinct red coloration close to the interface could be seen post-centrifugation, indicating that the NPs have successfully migrated to the LLI (Figure 2b). The NPs are known to provide an interfacial tension stabilization between the oil and water,[43] this stabilization also prevents the particles from crossing the LLI and

TABLE 1. Point by Point Summary of Experimental Procedures for the Assembly of NPs to the LLI and Measuring LSPR Maxima

experimental step	DCE volume (μL)	aqueous volume (μL)	description
(1) DCE saturation with H_2O	500	100	H_2O is added to DCE aliquot and emulsified by vigorous shaking.
(2) NP/NaCl solution preparation	0	1000	Separately, 500 μL NP solution is added to 500 μL NaCl solution (for NP/NaCl concentrations see Table 2).
(3) addition of NP solution to water-saturated DCE	500	600	500 μL of solution (2) is added to mixture (1) [the remainder of (2) is used to estimate the bulk NP concentration by UV—Vis spectroscopy].
(4) centrifugation	500	600	Mixture (3) is centrifuged, followed by gentle inverting to homogenize the bulk concentration of NPs.
(5) estimation of the number of NPs adsorbed at LLI	500	100	500 μL of mixture (4) is removed and used for UV—Vis to measure the residual bulk NP concentration, which allows estimation of the number of adsorbed NPs.
(6) background transmission measurement	500	100[a]	Mixture (1) is used to measure background transmission spectrum.
(7) LSPR at LLI measurement	500	100	The mixture remaining after stage (5) is used to measure LSPR of the NPs adsorbed to the LLI by transmission spectroscopy.[b]

[a] For transmission of droplets with a volume greater than 100 μL, the background was measured with the greater volume. [b] For volume- and pH-dependent experiments, these steps were initially carried out, followed by additional procedures as highlighted in the main text.

TABLE 2. Experimental Conditions, the Number of NPs, the NaCl Concentration, RCF, Time of Centrifugation, Aqueous Droplet Volume, and pH, for the Results Shown in Figures 3, 4, 6, and 7

experimental variable	total NPs in solution	NaCl concn (mM)	centrifugation speed - RCF (g)	centrifugation time (min)	aq. droplet volume (μL)	pH
NaCl concentration	2.75×10^{11}	(1—193)	9391	10	100	5.5
RCF	2.75×10^{11}	75	(93—13523)	10	100	5.5
centrifugation time	2.75×10^{11}	75	9391	(0.5—30)	100	5.5
droplet volume	2.75×10^{11}	75	9391	10	(100—300)	5.5
pH	2.75×10^{11}	165	9391	10	100	(2—9)

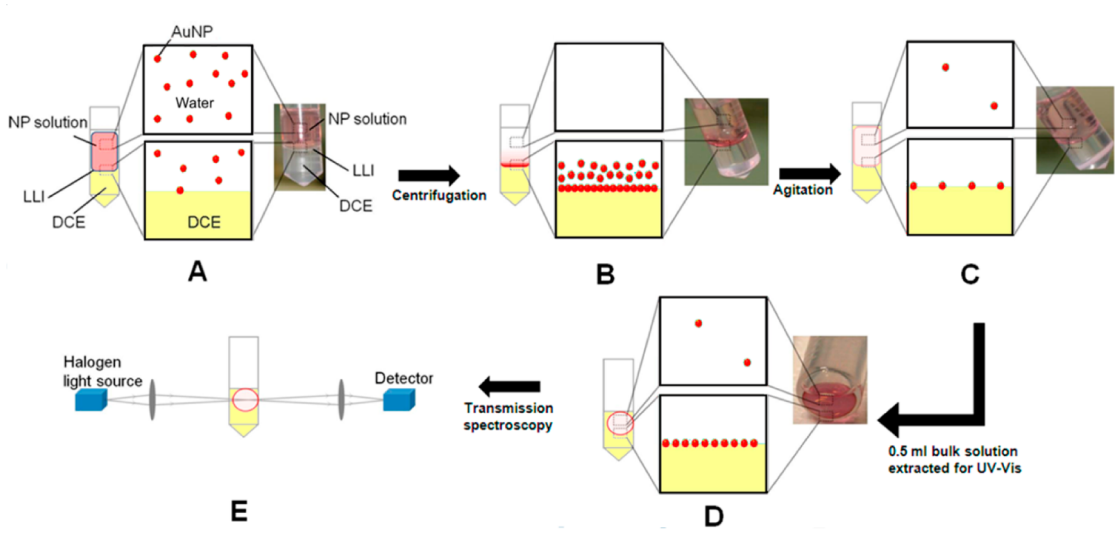

Figure 2. Schematic of the experimental procedure. All experiments were carried out with a 0.5 mL DCE and a 0.6 mL aq NP solution (A). Upon centrifugation (B), the centrifugal driving force provided a means to speed up NP adsorption at the LLI. (C) A total of 0.5 mL of the aqueous phase was then removed from the tubes, followed by gentle agitation of the remaining phases, readdition of the removed aq. phase followed again by removal of 0.5 mL aq phase for UV—Vis measurements (D). Remaining 100 μL droplet was then imaged by transmission spectroscopy in the geometry shown in (E).

sedimenting at the bottom of the DCE. However, as described, nanoparticles are charged and repel each other electrostatically unless this repulsion is substantially screened.[8] Consequently, these NPs could be visibly redispersed back into the bulk by gentle agitation at NaCl concentrations below 50 mM, while no visible change in the bulk occurred at NaCl concentrations above 50 mM. The NaCl concentration had a large effect on the visual appearance of the LLI. Between approximately 40—150 mM a highly glossy reflective film was observed at the LLI, at concentrations above 150 mM a matt appearance was observed while at concentrations below 40 mM only faint coloration was observed. It should be

stressed that the transitions do not have clear boundaries.

The remaining 100 μL of the aqueous phase formed a truncated oblate ellipsoid droplet whose surface area was estimated to be 1.071 $\pm$ 0.01 cm^2 in the cell holder (see Supporting Information for more details). Optical transmission spectra of the NPs at the aqueous droplet/DCE interface (Figure 2e) were measured to determine the localized surface plasmon resonance (LSPR) maxima, with a beam diameter of 1.5 mm at the sample interface. Before each reading, the sample height was adjusted so that the incident light would pass at approximately normal incidence; this was monitored by the intensity of the collected light, which decayed rapidly at non-normal incidences. The tube holder was tilted to approximately 5°, which minimized variations in the droplet shapes in the set of performed experiments. This tilt also helped to pin the droplets by buoyancy to an approximately constant position with respect to the incident light.

NP Functionality. It was found that functionalization groups play a large role in controlling the assembly of NPs at the LLI shown schematically in Figure 1c. The critical role of the functionality is well documented, with several works focusing on the role of the particle's surface chemistry on adsorption and behavior at the LLI.[44−46] For example, 12-mercaptododecanoic acid (MDDA)-functionalized particles do not spontaneously assemble in large quantities at the LLI at low salt concentrations. This is evidenced from the fact that the centrifugation and homogenization process leaves the vast majority of the NPs in the bulk solution. On the other hand, performing an identical experiment with citrate stabilized particles results in the majority of the available NPs adsorbed to the LLI. Unfortunately agglomeration readily occurs for citrate stabilized particles; therefore, they were not used for further experiments. The MDDA functionality prevents the adsorbed NPs from agglomerating as the carbon chain provides approximately a 1.5 nm steric coating that circumvents short-range van der Waals interactions which induce aggregation. Furthermore, the dissociated carboxyl groups at the end of the carbon chain provide a Coulombic repulsion. This stabilizing technique was extremely successful, so much so that no irreversible aggregation was observed at any conditions tested. The stabilizing effect of steric repulsion for particle suspensions is consistent with the literature.[47] It is known that purely electrostatically stabilized gold particles aggregate at salt concentrations greater than 20 mM.[48] Above these salt concentrations the Debye screening length is reduced such that the electrostatic repulsion can no longer overcome the van der Waals attraction forces between the NPs causing aggregation. However, due to the interplay of the additional forces that takes place at the LLI, as well as the interface-caused modification of electrostatic and van der Waals interactions, the signatures of the bulk aggregation cannot be directly used to extrapolate the salt effect on the electrostatic repulsion at a LLI.[34,49] It is beyond the scope of this work to further investigate this interplay as well as accurately describe the local ionic concentration surrounding NPs at the LLI. However, invaluable insight can be found in other works.[34,50] As for the effects of the steric and electrostatic stabilization, provided by the MDDA functionality, in comparison with a predominantly electrostatic stabilization by mercaptosuccinic acid for NPs at the LLI, they are qualitatively compared in Figure S3 of the SI.

Salt Concentration Dependence on NP Adsorption and Plasmon Resonance. The effect of ionic strength on the number of particles assembled at the LLI is shown in Figure 3a−d. This value can be assessed from both the residual NPs in the aqueous phase (Figure 3b) and the LSPR spectra (Figure 3a). A clear red shift was observed as the NaCl concentration was increased gradually from 1 to 200 mM. Between these NaCl concentrations, the Debye screening is reduced from approximately 9.6 to 0.7 nm. It should be noted that the Debye screening may not only affect the NP population at the interface, but their precise position relative to the boundary.

Two potentially competing sources of red-shifting can be attributed to the experimental observations. The first is a change in the dielectric constant of the surrounding medium of the NPs, while the second is plasmon coupling. The dielectric constant of pure water and a 2 M NaCl solution is 1.78 and 1.80, respectively. Therefore, even if the local salt concentration at the interface in the electrical double layer is 10 times that of the bulk, a negligible positional change of the LSPR maximum would be observed. DCE on the other hand has a dielectric constant of 2.09; therefore, a more substantial effect could result from the NPs position shifting from the aqueous to DCE phases. However, the shift in the position of the LSPR would be minor in contrast to the shift caused by the resulting change of the distance between the NPs at the LLI. As a result, the observed shift can be attributed to distant dependent plasmon coupling.

With no addition of NaCl (i.e., intrinsic ionic strength equivalent to 1 mM NaCl), the number of NPs that could be adsorbed to the LLI under an RCF of 9391 g in 10 min was 4.0 $\pm$ 0.1 $\times$ 10^{10} NPs from a bulk aqueous solution containing a total of 2.75 $\times$ 10^{11} NPs. The low ionic strength of the solution means that the electrostatic repulsion acts over a longer distance inhibiting oncoming particles from adsorbing to the interface. At these conditions, the LSPR maximum was 524 $\pm$ 3 nm, which corresponds to the LSPR maximum of the NPs in the bulk aqueous solution. This suggests that little to no plasmonic coupling occurs due to a large separation between NPs. Based on both the empirical plasmon ruler equation as well as mean-field theory, the spacing

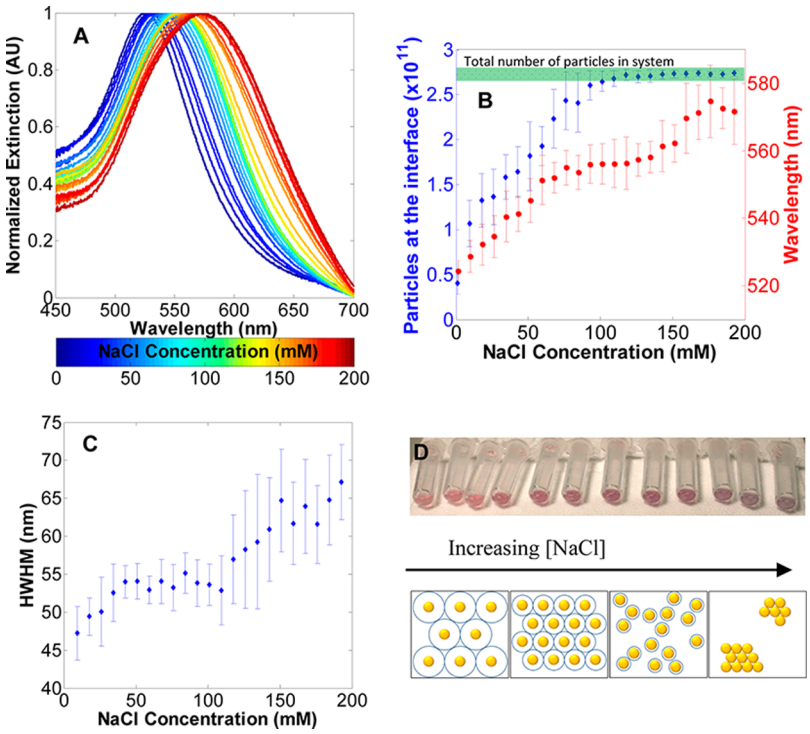

Figure 3. Dependence on plasmonic properties of 16 nm diameter gold NPs. (A) Full normalized spectra of samples. The spectra show a red-shift and peak broadening as the [NaCl] is increased. For clarity, the plasmon maximum with the number of particles adsorbed to the interface and half width at half-maximum are plotted in (B) and (C), respectively. A photograph of the samples (D) shows the effect of increasing the salt concentration on the NP color. Also included is a schematic showing the effect of increasing salt concentration on the nanoparticle spacing/arrangement.

is expected to be larger than 30 nm (Figure 5).[51,52] Increasing the salt concentration decreases the effective distance over which electrostatic repulsion takes place. As a result, a greater number of particles can be accommodated at the LLI. Because the surface area of the droplet and total number of particles in solution are roughly uniform, the spacing between NPs can be directly controlled by the addition of salt. This leads to a linear red-shift in the plasmonic response and a linear increase in the number of NPs adsorbed to the LLI between 1 and 75 mM NaCl. Between 75 and 125 mM NaCl both the LSPR maxima and the number of adsorbed particles plateaus at ≈555 nm and ≈2.75 × 10^{11} particles, respectively. This is due to all of the particles in the solution being collected at the interface. Under these conditions the average interparticle spacing remains constant. Finally, at concentrations above 150 mM NaCl, a further red-shift is observed. As the number of particles at the interface is already saturated, the red-shift is attributed to inhomogeneities and clustering of the NPs. This is supported by observing an increase in broadening of the plasmon spectra, Figure 3c. At lower salt concentration (1−50 mM) a linear dependence on the hwhm is observed, which is followed by a plateau between 50 and 110 mM and, finally, a second increase at concentrations >110 mM. By taking these observations into account along with the LSPR maxima and NP surface coverage, a possible explanation of these trends is shown in Figure 3d. As the NaCl is increased, NP coverage at the LLI will gradually go from a relatively ordered state to a disordered agglomerated state. This is further supported by the visual appearance of the LLI that, at low/moderate salt concentrations, appears golden mirror-like, which becomes matt in appearance at higher concentrations. The qualitative trends for red-shifting and peak broadening are as expected from the literature although broadening at higher NaCl concentrations is likely to be a combination of closer spacing and irregularities in the structure of the monolayer of NPs.[8,53]

In summary, based on the experimental results, NaCl concentrations of 1−75 mM give rise to controlled spacing with a relatively homogeneous NP distribution; the observed LSPR maximum at 75 mM NaCl is 555 ± 5 nm, which corresponds to a $\Delta\lambda/\lambda_0$ of ≈0.057. Coupled dipole approximation (CDA) simulations[52] suggest that a $\Delta\lambda/\lambda_0$ of 0.057 correlates to a gap distance/diameter of ≈0.65 which corresponds to ≈10 nm surface−surface NP separation in a hexagonal lattice (preferred packing geometry for a two-dimensional array of NPs with predominantly repulsive interactions). While mean-field theory[51] suggests that LSPR maximum of 555 nm corresponds to ≈4 nm. Our experimental data at these conditions suggests a surface−surface NP separation of ≈6 ± 1 nm (or a gap distance/diameter of ≈0.37), which lies between simulations and theory (Figure 5). Taking the

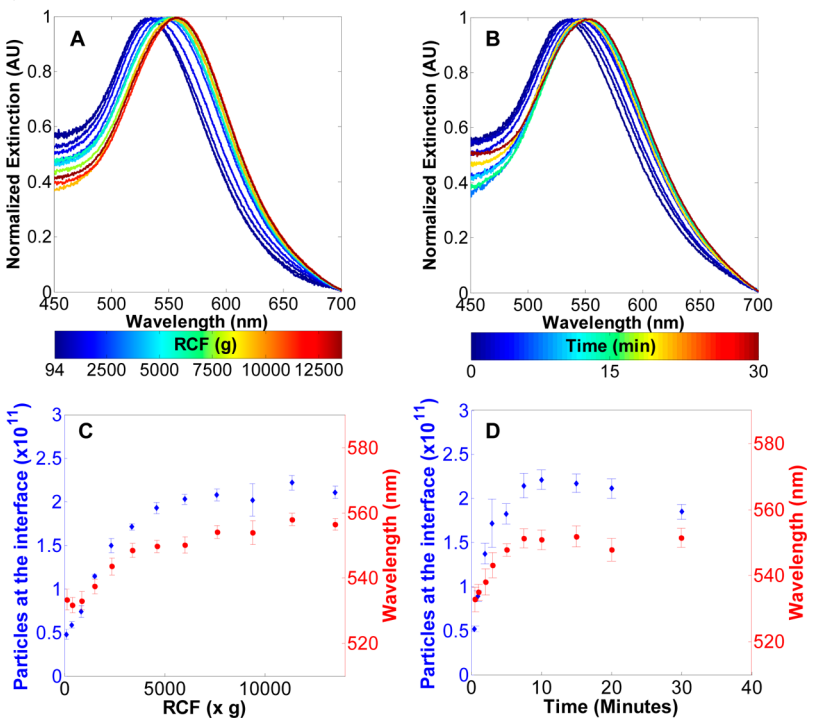

Figure 4. Transmission spectra as a function of RCF and centrifugation time are shown in (A) and (B). Corresponding LSPR maxima and number of particles adsorbed to the LLI are shown in (C) and (D) respectively.

steric coating of MDDA to be ≈1.5 nm and the Debye screening length to be 1.1 nm, then the minimum separation between 2 NPs is expected to be 5.2 nm; this is within experimental uncertainty of the experimentally determined values for NP separations at 75 mM.

Centrifugation Speed and Time Dependence on NP Adsorption and Plasmon Resonance. Centrifugation speed and time can also be used to control adsorption and the plasmonic properties of the NPs at the LLI (Figure 4). In Figure 4a,c the only parameter that was changed when compared to the NaCl results was the centrifugal force. The data shows very predictable behavior with a strong correlation between particle adsorbed to the interface and the plasmon red-shift. Both parameters increased until a plateau is reached which is a result of all particles being adsorbed to the interface. For example, the plasmon maximum at a RCF of 13523 g is 556 ± 2 nm ($\Delta\lambda/\lambda_0 \approx 0.059$), which corresponds to a 30 nm red-shift. Based on the plasmon ruler equation, $\Delta\lambda/\lambda_0 \approx 0.059$ suggests a ≈0.64 gap distance/diameter (or a ≈10 nm gap), while mean-field theory predicts a LSPR max of 556 nm corresponding to ≈4 nm surface−surface NP separation (Figure 5a,b).

The time-dependent studies (Figure 4b,d) show that, at short centrifugation times, a sharp increase in the number of particles adsorbed at the LLI is observed. This is followed by a plateau after 10 min where $2.2 \pm 0.1 \times 10^{11}$ NPs are adsorbed to the LLI. This is followed by a gradual decrease to a value of $1.8 \pm 0.2 \times 10^{11}$ NPs at 30 min is observed. This decrease could be attributed to heating of the samples that takes place during centrifugation, as dissociation is believed to be more efficient at higher temperatures, although further experiments are needed to verify this (*cf.* Figure 4d).

Combining the experimental data from Figures 3 and 4 (1−75 mM NaCl data), a plot of surface−surface NP separation can be drawn as a function of plasmon maximum (Figure 5a). Results from Figure 3 at NaCl concentrations of >75 mM were excluded due to the evidence of an inhomogeneous NP environment. The data presented is compared to two models. One of them was developed by Ben *et al.*[52] where a coupled dipole approach was used to calculate the plasmon frequency of an ordered 2D array of dipole scatterers. The results of these numerical calculations were then fit to a simple exponential function. However, one must be aware that the model cannot be directly applied to our system, because it was developed for an array of nanoparticles in vacuum; therefore, only the medium-independent $\Delta\lambda/\lambda_0$ can be used to compare qualitative trends (Figure 5b). In addition, we compare the results with a simple mean-field quasi-static dipolar theory developed by Kornyshev *et al.*[51] where we numerically determine the position of the plasmon resonance as a function of the distance between NPs (Figure 5a,b). The experimentally observed general trend is very similar to that predicted by both models. It is worth noting that deviation between the predictions of the mean-field theory and experimental RCF/time data becomes significant at larger interparticle separation due to a breakdown of the "continuous film" representation of the nanoparticle array.[51] The combined results from

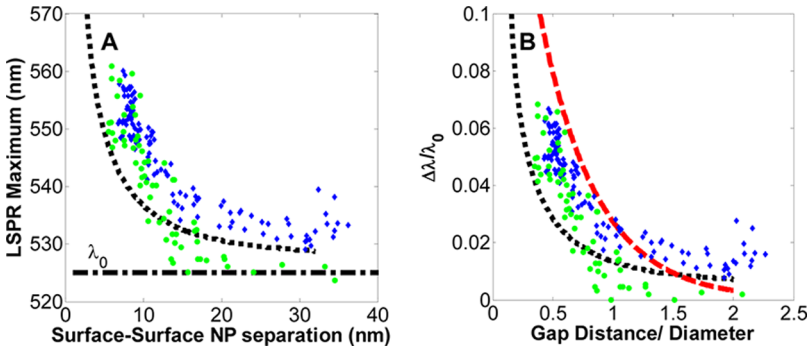

Figure 5. Demonstration of the plasmon ruler at the LLI for time- and RCF-dependent experiments (blue diamonds). NaCl-dependent experiments for concentrations ≤75 mM are also shown (green circles). The results from mean-field theory are shown as a black dotted line (A). Experimental results and theory are compared to CDA simulations (red dashed line). The LSPR shift is given as $\Delta\lambda/\lambda_0$, making the results applicable to Au NPs in any medium. The *x*-axis shows the dimensionless $a/2R$, the surface-to-surface separation divided by the diameter. λ_0 was taken to be 525 nm, as this represents the LSPR maximum of NPs in bulk water for the experimental results (B).

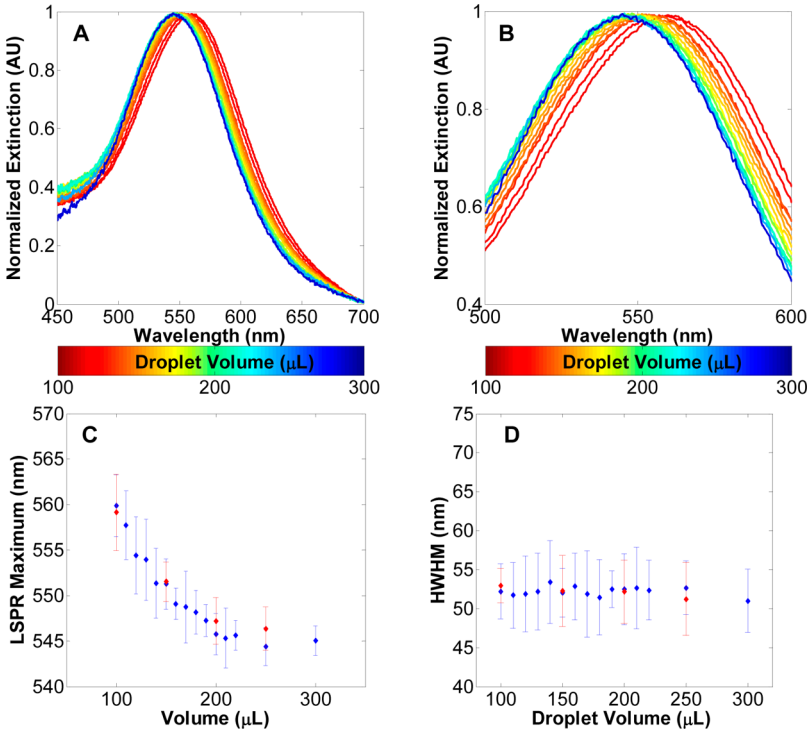

Figure 6. Volume dependence on transmission spectra (A, B), LSPR (C), and hwhm (D). Increasing the droplet volume leads to a blue shift (blue points). Importantly, the shift is reversible and a reduction of the volume (red points) results in the LSPR maxima going back to its original value.

the RCF and time-dependent studies suggest that the surface-to-surface separation between NPs can be precisely controlled between 7 and 30 nm, solely based on the centrifugation speed and time.

Volumetric Dependence on NP Adsorption and LSPR. Given that the results obtained from Figures 3 and 4 suggest that controlled spacing can be achieved, it follows naturally that one would expect to find a dependence on the LLI interfacial area for a constant total number of NPs at the interface. If the NPs' Coulombic as well as the long-range dipole−dipole repulsion lead to the NPs being spaced as far away from each other as possible at the LLI, then spacing should increase if the LLI area also increases. To verify this hypothesis, experiments were performed, increasing or decreasing the total aqueous droplet volume by pipetting fluid in or out of the droplet (Figure 6). The results suggest a clear dependence on the LSPR maximum with respect to the volume within a range of 100−200 μL. This is followed by a plateau at higher volumes. As expected, increasing the volume of the droplet causes a blue-shift in the LSPR maximum. For example, the LSPR maximum within a 100 μL was found to be 560 ± 3 nm, while 200 μL droplets had plasmon maxima of 546 ± 2 nm.

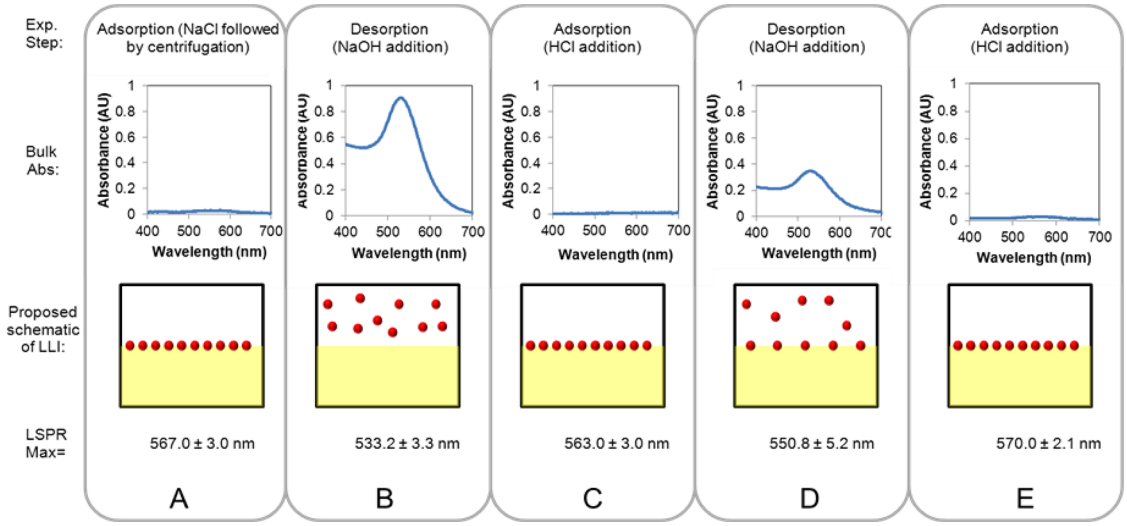

Figure 7. Demonstration of reversibility of NP adsorption/desorption. After assembly, the bulk salt was diluted in the aqueous phase 100× (A). Addition of 5 μL of 5 mM NaOH, followed by removal and combination of 5 μL from each of the 24 samples (B), with the position of the plasmon maximum shifting from 567.0 ± 3.0 to 533.2 ± 3.3 nm and the bulk absorption from UV−vis of ≈0.9. After the addition of 10 μL of 5 mM HCl, vigorous shaking of the sample and removal of 10 μL of the aqueous phase (C), the LSPR maximum from transmission returns to approximately the same value as the first adsorption step, while the bulk absorbance is negligible. Subsequent HCl/NaOH additions (D) and (E) show only partial reversibility.

The comparison of our experimental data with both models suggest that the surface-to-surface separation between NPs lies in the range of 6−13 nm. The decrease in the droplet volume, which results in a decrease in the LLI surface area, causes a red-shift in the LSPR maximum. It is important to note what happens when the volume is reduced below the initial 100 μL volume: the compression experienced by the particles initially leads to the expected red-shift, both visually and by transmission measurements; however, if the system is allowed to reach an equilibrium either by agitation or by waiting for a short period of time, then desorption of the "excess" NPs occurs. This is evidenced by both the LSPR maximum returning to ≈560 nm (*i.e.* same as for 100 μL) and the fact that after homogenization the NP in the bulk aqueous phase is greater than before homogenization. This is in marked contrast to close packed citrate stabilized arrays which are known to form `3D interfaces' and show buckling when the area of 2D NP array becomes larger than the area of the LLI.[54,55]

Reversibility of NPs at the LLI. NP adsorption at the LLI is impeded by electrostatic repulsion between the particles. For highly charged NPs there may be a barrier for individual NPs caused by resolvation. Both factors depend on the square of the charge of the NPs. Therefore we investigated the effect of changing the charge on the NPs to facilitate adsorption/desorption (Figure 7). NPs were assembled as described in Table 2. At this point, UV−Vis spectroscopy showed a negligible bulk absorbance (Figure 7a). The LSPR maximum was measured to be 567 ± 3 nm (consistent with the value at 165 mM NaCl from Figure 3b). To achieve desorption, 5 μL of 5 mM NaOH was added to the droplet, resulting in a final pH of approximately 9. This resulted in complete desorption of NPs from the LLI, which was evidenced by an increase in the bulk absorbance at 530 nm (Figure 7b). A blue-shift of the LSPR maximum (533 ± 3 nm) was also observed, which corresponds to the peak maxima for NPs in the bulk (530 nm).

Subsequent acidification of the aqueous solution with 10 μL of 5 mM HCl to a pH of approximately 2 and removal of the 10 μL "excess" aqueous phase (to ensure a constant volume) results in almost complete readsorption of the NPs (Figure 7c). The LSPR maximum returned to 563 ± 3 nm with UV−vis confirming that there was a negligible NP concentration in the bulk. Though this adsorption−desorption−adsorption cycle essentially suggests that full reversibility can be achieved, subsequent cycles could only demonstrate partial reversibility. The following desorption steps lead to a LSPR maximum of only 550.8 ± 5.2 nm and a bulk absorbance at 530 nm of ≈0.4, while the adsorption steps lead to negligible bulk NP concentration and an LSPR maximum of 570 ± 2 nm. This demonstrates an important step forward towards control of NP assemblies at the LLI, with the goal of coupling reversible adsorption with the plasmonic ruler by electrochemical means, that is, applying voltage across the ITIES, as suggested previously.[8]

CONCLUSIONS

We have demonstrated novel plasmonic properties of NPs localized at a LLI. Experimental results suggest that these properties arise from controlled spacing and that this spacing is affected by a set of controlled parameters. This was observed *indirectly* by normalized

transmission spectroscopy. Importantly, experimental results qualitatively agree with mean-field theory, as well as the empirical plasmon ruler equation. The unique properties of homogeneous, controlled, submonolayer coverage NP assemblies at the LLI open routes for many potential applications ranging from plasmonic rulers to detectors and electro-variable optics.

Whereas, the *indirect* imaging is, as demonstrated, a fast and convenient way to probe the structural properties of these assemblies, further experiments with *direct* imaging will be crucial to prove/disprove the spacing hypothesis as well as to provide a relatable reference point for the exact spacing. We believe that the results that we presented in this paper give motivation and framework to such studies. Aside from demonstrating a novel centrifugation-based assembly method and a noninvasive, *in situ* optical characterization of the forming assemblies, we have also shown reversibility of the adsorption of 16 nm diameter gold particles. Finally, we have obtained results suggesting that the structural properties of NPs that are already localized to the LLI can be fine-tuned by varying the interfacial area.

It is hoped that, due to the simplicity of the experimental procedure developed here to achieve adsorption, desorption, and controlled spacing, this work will provide convenient techniques to study the details of these assemblies, as well as pave the way to control these features *via* electrochemical means.

EXPERIMENTAL SECTION

Equipment used include the following: UV−Vis measurements to quantify the number of particles assembled at the inferface were performed with a Nanodrop 2000c spectrometer using PMMA cuvettes. An Eppendorf 5424 centrifuge was used to aid in self-assembly of Au nanoparticles using 2 mL polypropylene centrifuge tubes. A FA-45−24−11 rotor with a radius of 8.4 cm was used and is capable of holding 24 × 2 mL centrifuge tubes at an angle of 45° with a maximum relative centrifugal force (RCF) of 20238 g (14680 rpm). A Beckmann Coulter DelsaNano C dynamic light scattering machine was used for hydrodynamic particle sizing and zeta potential measurements. Broadband transmission spectra were obtained with a home-built optical setup, with the core components consisting of a miniature fiber optic spectrometer (Ocean Optics, S2000) and a Tungsten halogen light source (Micropack, HL-2000). This setup was used to measure the LSPR spectra and approximate the interparticle spacing. It is important to note that due to the geometry of the setup, the incident light passed through two NP interfaces (i.e., the interface was elliptical). A Leo Gemini 1525 FEGSEM scanning electron microscope was used to size the NPs as well as provide evidence of monolayer formation (rather than multilayers). A Mettler-Toledo SevenGo Duo pro pH/ion/conductivity meter was used for conductivity measurements.

In all cases, ultrapure water with a resistivity of 18.2 MΩ·cm was used. All chemicals were purchased from Sigma-Aldrich U.K. and used without further purification. Chemicals used include the following: $HAuCl_4 \cdot \approx 3H_2O$ (f.w. 339.79 (anhydrous), 99.999% trace metal basis); trisodium citrate dihydrate (f.w. 294.10, ≥99%); 12-mercaptododecanoic acid (MDDA, f.w. 232.38, 99%); ethanol (molecular biology, absolute grade); methanol (MeOH, CHROMASOLV, HPLC grade, ≥99.9%); sodium chloride (f.w. 58.44, ≥99.5%); 1,2-dichloroethane (DCE; ACS reagent, ≥99.0%).

MDDA Stabilized Gold Nanoparticle Synthesis. Gold NPs were synthesized based on the Turkevich-Frens recipes:[56,57] 8.6 mg $HAuCl_4 \cdot 3H_2O$ (5 mg gold) was dissolved in 95 mL of H_2O and brought to 100 °C. Under stirring, 5 mL of 13.6 mM sodium citrate solution was then added to the refluxing mixture. The initially faint-yellow solution gradually turned dark-blue, followed by wine-red over a period of 10 min. At this point, the NPs were measured to have a hydrodynamic diameter, electrophoretic mobility, and zeta potential of 20 ± 4 nm, -3.60×10^{-4} cm^2/(V s), and −47.0 mV, respectively. The size of the particles was verified to be ≈16 ± 3 nm using a SEM. Once the reaction had gone to completion (typically less than 15 min), the temperature was reduced to 60 °C. This was followed by the addition of MDDA (5 mg) dissolved in MeOH (0.5 mL). The functionalization was allowed to continue for at least 1 h to ensure complete monolayer coverage, after which the mixture was allowed to slowly cool under stirring for at least an extra hour. The excess MDDA precipitated out and was removed by filtration. The functionalized NP typically had a hydrodynamic diameter of 26 ± 7 nm, a conductivity of 217 μS/cm, electrophoretic mobility of -4.37×10^{-4} cm^2/(V s) and a zeta potential of −57.0 mV. The concentration of the NPs was then increased by centrifugation to the desired value. The "as-made" NP solution used for the experiments had an absorption of 0.890 at 525 nm. Taking an extinction coefficient of 4.92×10^8 M^{-1} cm^{-1}[58], the concentration of NPs was determined to be 1.8 nM or 1.09×10^{12} NPs/mL.

Conflict of Interest: The authors declare no competing financial interest.

Acknowledgment. We are thankful to Michael Urbakh, Michael Flatte, and Monica Marinescu for useful discussions. J.B.E. thanks the European Research Council starting grant scheme for financial support. A.A.K. also acknowledges support provided by FP7 EU grant "Nanodetector."

Supporting Information Available: A discussion of centrifugation, SEM images of dried nanoparticle arrays, the effects of the dielectric constant on the LSPR maximum, a comparison between mercaptosuccinic acid and MDDA, and details of the calculation of the interfacial area and HWHM. This material is available free of charge *via* the Internet at http://pubs.acs.org.

REFERENCES AND NOTES

1. Ramsden, W. Separation of Solids in the Surface-Layers of Solutions and Suspensions (Observations on Surface-Membranes, Bubbles, Emulsions, and Mechanical Coagulation): Preliminary Account. *Proc. R. Soc.* **1903**, *72*, 156–164.
2. Pickering, S. U. Emulsions. *J. Chem. Soc.* **1907**, *91*, 2021.
3. Yogev, D.; Efrima, S. Novel Silver Metal Liquidlike Films. *J. Phys. Chem.* **1988**, *92*, 5754–5760.
4. Kelly, K. L.; Coronado, E.; Zhao, L. L.; Schatz, G. C. The Optical Properties of Metal Nanoparticles: The Influence of Size, Shape, and Dielectric Environment. *J. Phys. Chem. B* **2002**, *107*, 668–677.
5. Duan, H.; Wang, D.; Sobal, N. S.; Giersig, M.; Kurth, D. G.; Möhwald, H. Magnetic Colloidosomes Derived from Nanoparticle Interfacial Self-Assembly. *Nano Lett.* **2005**, *5*, 949–952.
6. Younan, N.; Hojeij, M.; Ribeaucourt, L.; Girault, H. H. Electrochemical Properties of Gold Nanoparticles Assembly at Polarised Liquidliquid Interfaces. *Electrochem. Commun.* **2010**, *12*, 912–915.
7. Crossley, S.; Faria, J.; Shen, M.; Resasco, D. E. Solid Nanoparticles that Catalyze Biofuel Upgrade Reactions at the Water/Oil Interface. *Science* **2010**, *327*, 68–72.

8. Flatté, M. E.; Kornyshev, A. A.; Urbakh, M. Electrovariable Nanoplasmonics and Self-Assembling Smart Mirrors. *J. Phys. Chem. C* **2010**, *114*, 1735–1747.
9. Rotello, V. M.; Patra, D.; Malvankar, N.; Chin, E.; Tuominen, M.; Gu, Z. Y. Fabrication of Conductive Microcapsules *via* Self-Assembly and Crosslinking of Gold Nanowires at Liquid-Liquid Interfaces. *Small* **2010**, *6*, 1402–1405.
10. Kinnan, M. K.; Chumanov, G. Plasmon Coupling in Two-Dimensional Arrays of Silver Nanoparticles: II. Effect of the Particle Size and Interparticle Distance. *J. Phys. Chem. C* **2010**, *114*, 7496–7501.
11. Boker, A.; He, J.; Emrick, T.; Russell, T. P. Self-Assembly of Nanoparticles at Interfaces. *Soft Matter* **2007**, *3*, 1231–1248.
12. Benjamin, I. Theoretical Study of the Water/1, 2-Dichloroethane Interface: Structure, Dynamics, and Conformational Equilibria at the Liquid−Liquid Interface. *J. Chem. Phys.* **1992**, *97*, 1432.
13. Sonnichsen, C.; Reinhard, B. M.; Liphardt, J.; Alivisatos, A. P. A Molecular Ruler Based on Plasmon Coupling of Single Gold and Silver Nanoparticles. *Nat. Biotechnol.* **2005**, *23*, 741–745.
14. Jain, P. K.; Huang, W.; El-Sayed, M. A. On the Universal Scaling Behavior of the Distance Decay of Plasmon Coupling in Metal Nanoparticle Pairs: A Plasmon Ruler Equation. *Nano Lett.* **2007**, *7*, 2080–2088.
15. Su, K. H.; Wei, Q. H.; Zhang, X.; Mock, J. J.; Smith, D. R.; Schultz, S. Interparticle Coupling Effects on Plasmon Resonances of Nanogold Particles. *Nano Lett.* **2003**, *3*, 1087–1090.
16. Yang, L.; Wang, H.; Yan, B.; Reinhard, B. R. M. Calibration of Silver Plasmon Rulers in the 1−25 nm Separation Range: Experimental Indications of Distinct Plasmon Coupling Regimes. *J. Phys. Chem. C* **2010**, *114*, 4901–4908.
17. Liu, N.; Hentschel, M.; Weiss, T.; Alivisatos, A. P.; Giessen, H. Three-Dimensional Plasmon Rulers. *Science* **2011**, *332*, 1407–1410.
18. Gordon, K. C.; McGarvey, J. J.; Taylor, K. P. Enhanced Raman Scattering from Liquid Metal Films Formed from Silver Sols. *J. Phys. Chem.* **1989**, *93*, 6814–6817.
19. Wang, L.; Sun, Y.; Che, G.; Li, Z. Self-Assembled Silver Nanoparticle Films at an Air−Liquid Interface and Their Applications in SERS and Electrochemistry. *Appl. Surf. Sci.* **2011**, *257*, 7150–7155.
20. Zhang, J.; Coulston, R. J.; Jones, S. T.; Geng, J.; Scherman, O. A.; Abell, C. One-Step Fabrication of Supramolecular Microcapsules from Microfluidic Droplets. *Science* **2012**, *335*, 690–694.
21. Flatte, M. E.; Kornyshev, A. A.; Urbakh, M. Nanoparticles at Electrified Liquid−Liquid Interfaces: New Options for Electro-Optics. *Faraday Discuss.* **2009**, *143*, 109–115.
22. Pieranski, P. Two-Dimensional Interfacial Colloidal Crystals. *Phys. Rev. Lett.* **1980**, *45*, 569–572.
23. Hurd, A. J. The Electrostatic Interaction between Interfacial Colloidal Particles. *J. Phys. A* **1985**, *18*, L1055.
24. Tay, K. A.; Bresme, F. Wetting Properties of Passivated Metal Nanocrystals at Liquid−Vapor Interfaces: A Computer Simulation Study. *J. Am. Chem. Soc.* **2006**, *128*, 14166–14175.
25. Luo, M. Effects of Methanol on Nanoparticle Self-Assembly at Liquid-Liquid Interfaces: A Molecular Dynamics Approach. *J. Chem. Phys.* **2009**, *131*, 194703.
26. Reincke, F.; Kegel, W. K.; Zhang, H.; Nolte, M.; Wang, D.; Vanmaekelbergh, D.; Mohwald, H. Understanding the Self-Assembly of Charged Nanoparticles at the Water/Oil Interface. *Phys. Chem. Chem. Phys.* **2006**, *8*, 3828–3835.
27. Vermant, J.; Grzelczak, M.; Furst, E. M.; Liz-Marzan, L. M. Directed Self-Assembly of Nanoparticles. *ACS Nano* **2010**, *4*, 3591–3605.
28. Park, B. J.; Pantina, J. P.; Furst, E. M.; Oettel, M.; Reynaert, S.; Vermant, J. Direct Measurements of the Effects of Salt and Surfactant on Interaction Forces between Colloidal Particles at Water−Oil Interfaces. *Langmuir* **2008**, *24*, 1686–1694.
29. Park, B. J.; Vermant, J.; Furst, E. M. Heterogeneity of the Electrostatic Repulsion between Colloids at the Oil−Water Interface. *Soft Matter* **2010**, *6*, 5327–5333.
30. Flatté, M. E.; Kornyshev, A. A.; Urbakh, M. Understanding Voltage-Induced Localization of Nanoparticles at a Liquid−Liquid Interface. *J. Phys.: Condens. Matter* **2008**, *20*, 073102.
31. Boneva, M. P.; Danov, K. D.; Christov, N. C.; Kralchevsky, P. A. Attraction between Particles at a Liquid Interface Due to the Interplay of Gravity- and Electric-Field-Induced Interfacial Deformations. *Langmuir* **2009**, *25*, 9129–9139.
32. Williams, D. F.; Berg, J. C. The Aggregation of Colloidal Particles at the Air−Water Interface. *J. Colloid Interface Sci.* **1992**, *152*, 218–229.
33. Lehle, H.; Oettel, M. Importance of Boundary Conditions for Fluctuation-Induced Forces between Colloids at Interfaces. *Phys. Rev. E* **2007**, *75*, 011602.
34. Bresme, F.; Oettel, M. Nanoparticles at Fluid Interfaces. *J. Phys.: Condens. Matter* **2007**, *19*, 413101.
35. Singh, P.; Joseph, D. D.; Aubry, N. Dispersion and Attraction of Particles Floating on Fluid-Liquid Surfaces. *Soft Matter* **2010**, *6*, 4310–4325.
36. Lin, Y.; Böker, A.; Skaff, H.; Cookson, D.; Dinsmore, A. D.; Emrick, T.; Russell, T. P. Nanoparticle Assembly at Fluid Interfaces: Structure and Dynamics. *Langmuir* **2004**, *21*, 191–194.
37. Galletto, P.; Girault, H. H.; Gomis-Bas, C.; Schiffrin, D. J.; Antoine, R.; Broyer, M.; Brevet, P. F. Second Harmonic Generation Response by Gold Nanoparticles at the Polarized Water/2-Octanone Interface: from Dispersed to Aggregated Particles. *J. Phys.: Condens. Matter* **2007**, *19*, 375108.
38. Hojeij, M.; Younan, N.; Ribeaucourt, L.; Girault, H. H. Surface Plasmon Resonance of Gold Nanoparticles Assemblies at Liquid−Liquid Interfaces. *Nanoscale* **2010**, *2*, 1665–1669.
39. Zang, D.; Stocco, A.; Langevin, D.; Wei, B.; Binks, B. P. An Ellipsometry Study of Silica Nanoparticle Layers at the Water Surface. *Phys. Chem. Chem. Phys.* **2009**, *11*, 9522–9529.
40. Isa, L.; Lucas, F.; Wepf, R.; Reimhult, E. Measuring Single-Nanoparticle Wetting Properties by Freeze-Fracture Shadow-Casting Cryo-Scanning Electron Microscopy. *Nat. Commun.* **2011**, *2*, 1–9.
41. Su, B.; Abid, J.-P.; Fermín, D. J.; Girault, H. H.; Hoffmannová, H.; Krtil, P.; Samec, Z. Reversible Voltage-Induced Assembly of Au Nanoparticles at Liquid−Liquid Interfaces. *J. Am. Chem. Soc.* **2003**, *126*, 915–919.
42. Li, Y.-J.; Huang, W.-J.; Sun, S.-G. A Universal Approach for the Self-Assembly of Hydrophilic Nanoparticles into Ordered Monolayer Films at a Toluene/Water Interface. *Angew. Chem., Int. Ed.* **2006**, *45*, 2537–2539.
43. Du, K.; Glogowski, E.; Emrick, T.; Russell, T. P.; Dinsmore, A. D. Adsorption Energy of Nano- and Microparticles at Liquid−Liquid Interfaces. *Langmuir* **2010**, *26*, 12518–12522.
44. Isa, L.; Amstad, E.; Schwenke, K.; Del Gado, E.; Ilg, P.; Kroger, M.; Reimhult, E. Adsorption of Core-Shell Nanoparticles at Liquid−Liquid Interfaces. *Soft Matter* **2011**, *7*, 7663–7675.
45. Stefaniu, C.; Chanana, M.; Ahrens, H.; Wang, D.; Brezesinski, G.; Mohwald, H. Conformational Induced Behaviour of Copolymer-Capped Magnetite Nanoparticles at the Air/Water Interface. *Soft Matter* **2011**, *7*, 4267–4275.
46. D'Souza Mathew, M.; Manga, M. S.; Hunter, T. N.; Cayre, O. J.; Biggs, S. Behavior of pH-Sensitive Core Shell Particles at the Air−Water Interface. *Langmuir* **2012**, *28*, 5085–5092.
47. Reed, K. M.; Borovicka, J.; Horozov, T. S.; Paunov, V. N.; Thompson, K. L.; Walsh, A.; Armes, S. P. Adsorption of Sterically Stabilized Latex Particles at Liquid Surfaces: Effects of Steric Stabilizer Surface Coverage, Particle Size, and Chain Length on Particle Wettability. *Langmuir* **2012**, *28*, 7291–7298.
48. Meyer, M.; Le Ru, E. C.; Etchegoin, P. G. Self-Limiting Aggregation Leads to Long-Lived Metastable Clusters in Colloidal Solutions. *J. Phys. Chem. B* **2006**, *110*, 6040–6047.
49. Isa, L.; Amstad, E.; Textor, M.; Reimhult, E. Self-Assembly of Iron Oxide-Poly(ethylene glycol) CoreShell Nanoparticles at Liquid Liquid Interfaces. *Chimia* **2010**, *64*, 145–149.

50. Starov, V. M. *Nanoscience: Colloidal and Interfacial Aspects*; CRC: Boca Raton, FL, 2010.
51. Kornyshev, A. A.; Marinescu, M.; Paget, J.; Urbakh, M. Reflection of Light by Metal Nanoparticles at Electrodes. *Phys. Chem. Chem. Phys.* **2012**, *14*, 1850–1859.
52. Ben, X.; Park, H. S. Size Dependence of the Plasmon Ruler Equation for Two-Dimensional Metal Nanosphere Arrays. *J. Phys. Chem. C* **2011**, *115*, 15915–15926.
53. Zhao, L.; Kelly, K. L.; Schatz, G. C. The Extinction Spectra of Silver Nanoparticle Arrays: Influence of Array Structure on Plasmon Resonance Wavelength and Width. *J. Phys. Chem. B* **2003**, *107*, 7343–7350.
54. Tseng, T.-C.; McGarrity, E. S.; Kiel, J. W.; Duxbury, P. M.; Mackay, M. E.; Frischknecht, A. L.; Asokan, S.; Wong, M. S. Three-Dimensional Liquid Surfaces through Nanoparticle Self-Assembly. *Soft Matter* **2010**, *6*, 1533–1538.
55. Aveyard, R.; Clint, J. H.; Nees, D.; Quirke, N. Structure and Collapse of Particle Monolayers under Lateral Pressure at the Octane/Aqueous Surfactant Solution Interface. *Langmuir* **2000**, *16*, 8820–8828.
56. Turkevich, J. A Study of the Nucleation and Growth Processes in the Synthesis of Colloidal Gold. *Discuss. Faraday Soc.* **1951**, *11*, 55.
57. Frens, G. Controlled Nucleation for the Regulation of the Particle Size in Monodisperse Gold Suspensions. *Nature* **1973**, *241*, 20.
58. Liu, X.; Atwater, M.; Wang, J.; Huo, Q. Extinction Coefficient of Gold Nanoparticles with Different Sizes and Different Capping Ligands. *Colloids Surf., B* **2007**, *58*, 3–7.